APPLIED SCIENCES AND ENGINEERING

Mixed-dimensional MXene-hydrogel heterostructures for electronic skin sensors with ultrabroad working range

Yichen Cai[1]*, Jie Shen[2]*, Chi-Wen Yang[1], Yi Wan[1], Hao-Ling Tang[1], Areej A. Aljarb[1], Cailing Chen[2], Jui-Han Fu[1], Xuan Wei[1], Kuo-Wei Huang[1], Yu Han[2], Steven J. Jonas[3,4†], Xiaochen Dong[5†], Vincent Tung[1†]

Skin-mountable microelectronics are garnering substantial interest for various promising applications including human-machine interfaces, biointegrated devices, and personalized medicine. However, it remains a critical challenge to develop e-skins to mimic the human somatosensory system in full working range. Here, we present a multifunctional e-skin system with a heterostructured configuration that couples vinyl-hybrid-silica nanoparticle (VSNP)–modified polyacrylamide (PAM) hydrogel with two-dimensional (2D) MXene through nano-bridging layers of polypyrrole nanowires (PpyNWs) at the interfaces, featuring high toughness and low hysteresis, in tandem with controlled crack generation and distribution. The multidimensional configurations endow the e-skin with an extraordinary working range (2800%), ultrafast responsiveness (90 ms) and resilience (240 ms), good linearity (800%), tunable sensing mechanisms, and excellent reproducibility. In parallel, this e-skin platform is capable of detecting, quantifying, and remotely monitoring stretching motions in multiple dimensions, tactile pressure, proximity sensing, and variations in temperature and light, establishing a promising platform for next-generation smart flexible electronics.

INTRODUCTION

Mechanically robust and adaptive, elastic sensing microelectronics [i.e., electronic skin (e-skin)] with portability, foldability, and biocompatibility are highly desirable for emerging technologies and biointegrated devices, including next-generation prosthetics, soft robotics, human-machine interfaces, and personalized healthcare systems (*1*–*3*). An ideal engineered e-skin system should accurately mimic the properties of natural skin in real time (e.g., discriminate and evaluate multiple external stimuli and electrophysiologies), enabling users to interact and communicate with their surroundings and perform complex tasks in response to the users' instructions (*4*). This engineering challenge motivates the development of new materials, rational device architectures, and manufacturing methods to meet these capabilities successfully and collectively (*1*–*3*, *5*, *6*). Two-dimensional (2D) titanium carbide ($Ti_3C_2T_x$), a material from the metallically conductive MXene family (2D transition metal carbides and nitrides), has demonstrated state-of-the-art performance in electromagnetic interference shielding (*7*, *8*), energy storage (*9*, *10*), and electrocatalysis (*11*). Recent discoveries of exceptional mechanical properties (*12*, *13*) and extraordinarily high photothermal conversion efficiency around 100% (*14*, *15*) generated huge interest in the possible implementation of MXene in next-generation e-skin sensors.

Owing to the unique solution processability imparted by the abundant hydrophilic groups, existing MXene-based e-skin sensors are typically manufactured via embedding MXene as a filler into elastomers/gels (*16*, *17*). Although relatively easier to prepare, it may not be possible to mix the two materials uniformly, resulting in lamellar accumulation and agglomeration within the base gels. The nonuniformity issue also has an unintended consequence on the performance that greatly hinges on the orientation and stacking of MXene nanosheets. Moreover, previous studies on single-networked or metal ion–modified polyvinyl alcohol (PVA) hydrogel have collectively indicated that the reliable stretchability (elastic deformation) of PVA gel is around 1000% (*18*, *19*). Larger strain (>1000%) leads to an inelastic stretch phase in which the elastomer takes a very long time to recover or even catastrophically fails without recovery (*20*). Therefore, the advantageous feat of superior stretchability did not necessarily translate to the broad working range. Instead, the reliably working range of the MXene-PVA hydrogel sensor (different from stretchability) is limited to only 40% reported by Zhang *et al.* (*17*) and cannot meet the requirements for biological skin (~75%) or even for free movement of the knees, which experience surface strains up to 55%. Compounding the limited working range, the instantaneous resilience also abruptly fades when the strain exceeds 40% (*17*). It is also important to note that hydrogel substrates for e-skin sensors are required to dissipate as little energy as possible during normal operation of cyclic loads (low hysteresis) while dissipating much energy to resist rupture (high toughness) and surviving prolonged cyclic loads (fatigue resistant) (*21*). However, most of the hydrogels reported to date cannot meet these requirements simultaneously and often exhibit a very large hysteresis (*21*). It is therefore necessary to engineer hydrogels capable of disrupting the critical toughness-hysteresis correlation while leveraging highly dynamic working range, fast response, and excellent recovery properties before these materials can be well used as substrates in e-skin systems.

Here, we report an e-skin system that hinges on heterogeneously integrating a vinyl silica nanoparticle–polyacrylamide (VSNP-PAM)

[1]Physical Science and Engineering Division, Material Science and Engineering Program, King Abdullah University of Science and Technology (KAUST), Thuwal 23955-6900, Kingdom of Saudi Arabia. [2]Physical Science and Engineering Division, Advanced Membranes and Porous Materials Center, King Abdullah University of Science and Technology (KAUST), Thuwal 23955-6900, Kingdom of Saudi Arabia. [3]Department of Pediatrics, David Geffen School of Medicine, University of California, Los Angeles, Los Angeles, CA 90095, USA. [4]California NanoSystems Institute, University of California, Los Angeles, Los Angeles, CA 90095, USA. [5]School of Chemistry and Materials Science, Nanjing University of Information Science and Technology, Nanjing 210044, China.
*These authors contributed equally to this work.
†Corresponding author. Email: sjjonas@mednet.ucla.edu (S.J.J.); iamxcdong@njtech.edu.cn (X.D.); vincent.tung@kaust.edu.sa (V.T.)

hydrogel as the robust elastic substrate in conjunction with the orthogonally buckled sensing arrays composed of 2D MXene nanosheets and 1D polypyrrole nanowires (PpyNWs) in a layer-by-layer fashion. Specifically, spatially abundant hydrogen bonding between amide moieties on PAM chains and the covalent bonding between PAM and VSNPs can synergistically balance energy dissipation within VSNP-PAM hydrogel networks to achieve high toughness and low hysteresis simultaneously, currently unachievable by any state-of-the-art hydrogels. The result is a combination of high toughness (~7020 J/m^2) and very low hysteresis (<0.1), providing the e-skin sensor with fast responsiveness (~90 ms) and outstanding resilience (~240 ms). In parallel, the high stretchability of VSNP-PAM hydrogel can be neatly repurposed to harness the mechanical instabilities of 2D MXene nanosheets and 1D PpyNWs adhered on the prestretched VSNP-PAM hydrogel, affording tailored self-organized hierarchical structures. This is accomplished by the controlled relaxation of the prestrains in a particular order. Upon stretching, these hierarchically crumpled structures can be reflattened back to their original morphology, providing a route to MXene-PpyNW sensing components with functionality over broad working range. The introduction of 1D PpyNWs further preserves the structural integrity between the interfaces of VSNP-PAM and 2D MXene nanosheets while providing skin-like functionality and sensibility over the broad work range. This is made possible by the formation of dynamic linkages that synergistically combine topological entanglement, hydrophobic intercalation, and multiple hydrogen bonding. Despite the lack of chemical bonding between each component within the e-skin, the heterogeneous integration is proven to be intrinsically robust in nature. The resultant e-skin offers control over the stepwise propagating microcracks under mechanical deformation, ultrabroad working range (0 to 2800%), outstanding linear range (0 to 800% strain), reliable sensitivity [gauge factor (GF)] at large strain ($\varepsilon \sim 15$, GF of 16.9 in the *x* direction and 11.2 in the *y* direction), and excellent reproducibility (>5000 cycles). In addition, the sensing mechanism can be tuned from piezoresistive to capacitive effect by laminating two heterostructure networks together, enabling the capability of sensing tactile stimuli in *x*, *y*, and *z* directions and perceiving the proximity of others from a far distance of 20 cm. Other functions such as remote wireless transmission, temperature, and photoelectronic effects are also demonstrated.

RESULTS

Hydrogel fabrication

We synthesized highly stretchable and tough hydrogels that incorporate VSNPs to form VSNP-PAM (Figs. 1 and 2A). A sol-gel method was used to prepare VSNPs (Fig. 2B). It should be noted that unlike conventional approaches to synthesize PAM hydrogels (*5*, *22*), no cross-linker (i.e., *N*,*N*′-methylenebisacrylamide) was used in this experiment. Instead, the radical grafting polymerization process is thermally initiated at the vinyl groups on the surface of the VSNPs. The result is the formation of grafted polymer chains with one terminus attached to VSNPs, and the rest retains the freedom to interact with other polymer chains to form a nanobrush gelator. After introduction of ammonium persulfate as an initiator, the intermolecular

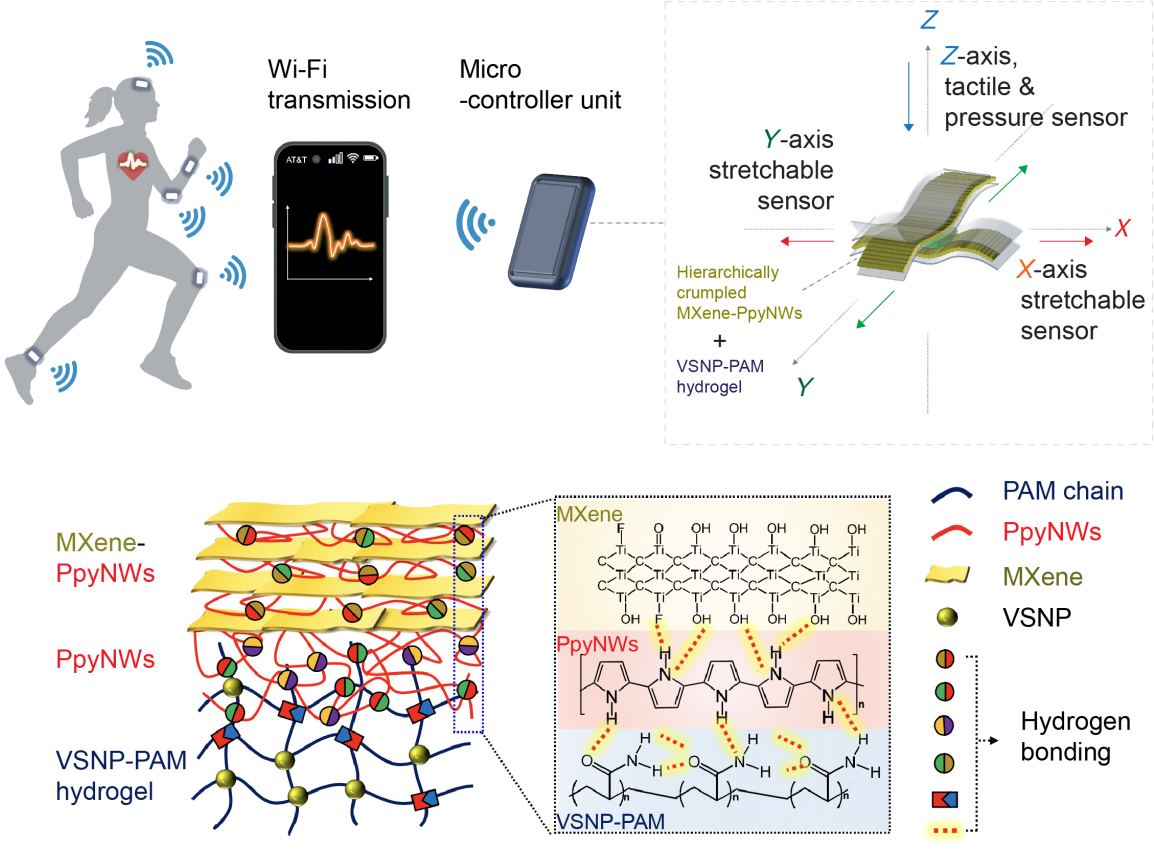

Fig. 1. Schematic illustration depicts the heterogeneous integrated e-skin that comprises MXene-PpyNW-VSNP-PAM in a layer-by-layer fashion.

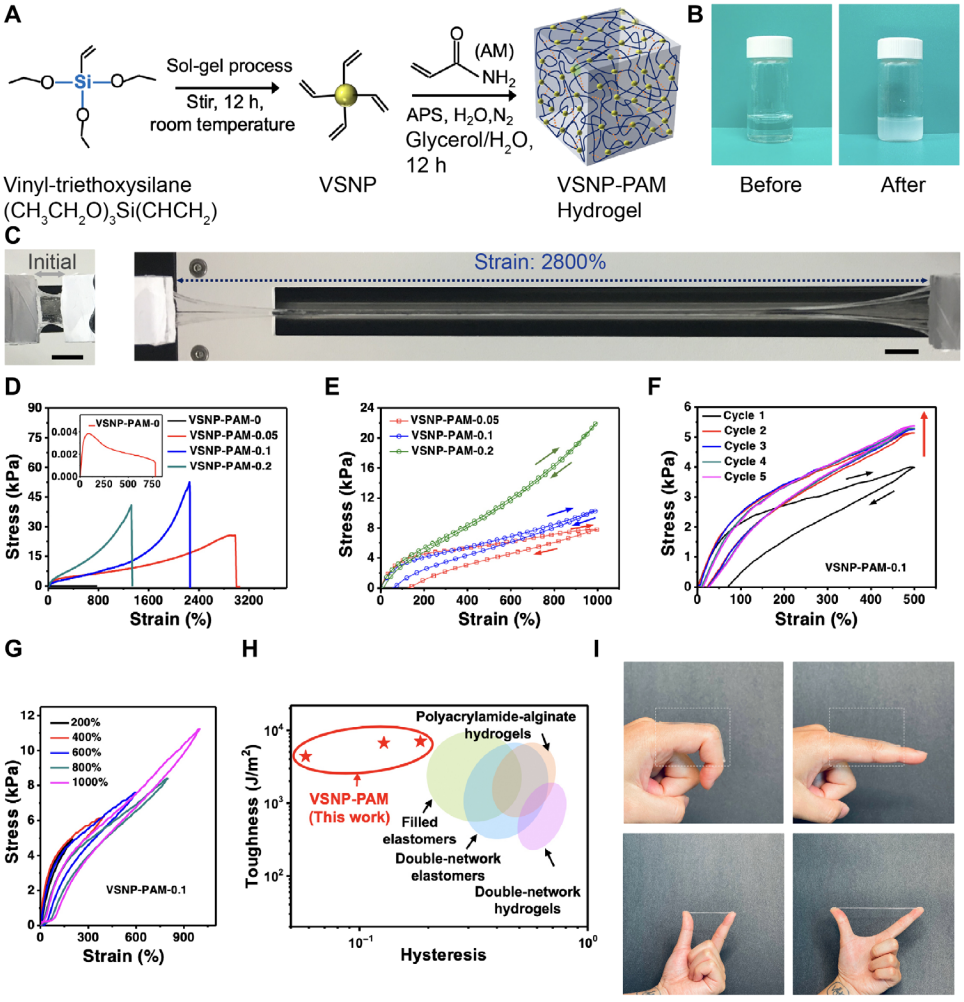

Fig. 2. Synthesis of the stretchable VSNP-PAM hydrogels with high toughness and low hysteresis. (**A**) Schematic representation of the synthetic procedure of VSNP-PAM hydrogels and their network-like structures. APS, ammonium persulfate. (**B**) Photographs of the as-synthesized VSNPs: Before (left) and after (right) the sol-gel process. Photo credit: Jie Shen and Yichen Cai, KAUST. (**C**) Initial (left) and elongated (right) states of the VSNP-PAM showcase the excellent stretchability (scale bars, 1 cm). Photo credit: Yichen Cai and Vincent Tung, KAUST. (**D**) Stress-strain curves for VSNP-PAM hydrogels with different VSNP contents. (**E**) Loading-unloading tensile curves of VSNP-PAM-*x* hydrogels at a strain of 1000%. Loading-unloading tensile curves of VSNP-PAM-0.1 at (**F**) different cycles and (**G**) different strains. (**H**) Toughness-hysteresis diagram benchmarks our work with current state-of-the-art hydrogels and elastomers. (**I**) A series of photographs show the compliant and viscoelastic nature of the VSNP-PAM hydrogels. Photo credit: Vincent Tung, KAUST.

hydrogen bonding between repeated acrylamide (AM) units and chemical cross-linking points of VSNPs leads to the formation of VSNP-PAM hydrogels. Therefore, the VSNPs could spontaneously serve as multifunctional chemical cross-linking points in the gels to balance their energy dissipation. Furthermore, VSNP-PAM can undergo a gel-sol transition if these cross-linking points are disrupted due to the fact that networks of hydrogel are held by intermolecular hydrogen bonding. The resultant VSNP-PAM hydrogels were transferred to a mixed solution of deionized water (DI-H_2O) and glycerol to exchange the solvents. This step endows the hydrogel with enhanced resistance to dehydration. When the VSNP-PAM is stretched (Fig. 2C and fig. S1), these covalent cross-linking points act as stress transfer centers, strengthening the networks, while the nonsacrificial hydrogen bonding can dynamically recombine to dissipate energy and homogenize the network under stretching.

The content of VSNPs strongly influences the toughness and hysteresis properties of the hydrogel. To obtain the high-toughness-and-low-hysteresis hydrogel, the VSNP content was varied systematically. Here, gels are designated as VSNP-PAM-*x*, where *x* denotes the content of VSNPs expressed as the weight percentage with respect to the weight of monomer (AM) used in the gel preparation process. When the VSNP content rises from 0 to 0.2 weight % (wt %), the VSNP-PAM hydrogels show a notable increase of breaking strain (maximum of 2800% at 0.05 wt %) and tensile strength (maximum of 52.5 kPa at 0.1 wt %), followed by a decrease (Fig. 2D and figs. S2 and S3), which is the result of the increased cross-linking site density and shortened polymer chains. Tensile strengths and break strains of hybrid gels are all higher than those of pure PAM (fig. S3). These results indicate that the mechanical properties of the hydrogel are tunable over a wide range, enabling more selectivity and adjustability when applied to e-skin sensing elements.

Comparing the tensile hysteresis curves of VSNP-PAM at the same strain of 1000% (Fig. 2E), VSNP-PAM with a higher content of VSNPs shows extremely smaller hysteresis loops because of the high density of cross-linking sites from VSNPs. In addition, fatigue resistance is

needed to sustain cyclic actuations in practical applications (*23*). On the basis of optimized toughness and hysteresis, we chose the VSNP-PAM-0.1 to measure the fatigue resistance through consecutive loading-unloading cycle tests at a maximum strain of 500% without resting between two tests (Fig. 2F). It becomes apparent that areas of hysteresis loops of VSNP-PAM-0.1 remained mostly constant for the following successive loading-unloading cycles after the first cycle, indicating unchanged dissipated energies. Figure 2G also shows the stable hysteresis loops of VSNP-PAM-0.1 under different strains. These results combined with the durability tests (shown in the sensory measurements) suggest that our modified VSNP-PAM could be used as an ideal antifatigue substrate, which can ensure durability and reliability in practical sensing applications. The toughness-hysteresis data of the representative stretchable materials are plotted in Fig. 2H for comparison (*21*). The toughness-hysteresis correlation corresponds to the diagonal region, and the conflicting requirements of high toughness and low hysteresis correspond to the upper-left quadrant (*21*). Although most of the existing hydrogel-based elastomers show a high hysteresis, our VSNP-PAM-0.1 hydrogel has high toughness (as high as 7020 J/m^2) and low hysteresis (even smaller than 0.1) concurrently, indicating a new niche in the stretchable material parameter space. Although polydimethylsiloxane (PDMS) composites and natural rubber show similar toughness-hysteresis behaviors (*24*), their implementation in e-skin is largely constrained by low stretchability, mismatched Young's modulus to skin, poor fatigue resistance, and biocompatibility. Photographs in Fig. 2I illustrate the VSNP-PAM hydrogel attached and conformed to a subject's fingers, indicating the excellent compliance and viscoelasticity, which is suitable for e-skin applications. Furthermore, the dehydration test was conducted, and the results are shown in figs. S4 and S5.

Assembly of e-skin devices

Figure 3A illustrates the procedure used to fabricate stretchable and compressible e-skins on the optically clear, high-toughness-and-low-hysteresis hydrogel (VSNP-PAM-0.1). We chose $Ti_3C_2T_x$ as the active

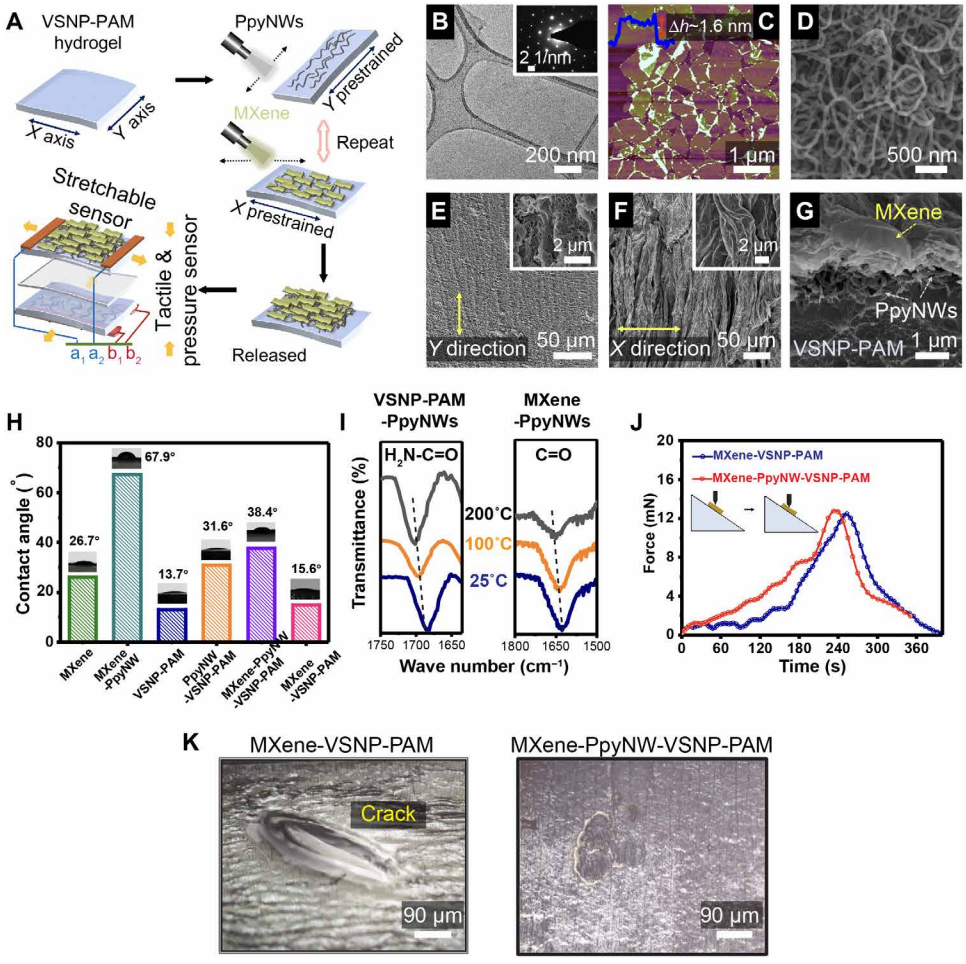

Fig. 3. Manufacturing of heterogeneously integrated e-skin and characterizations of the dynamic linkages at various interfaces. (**A**) A schematic illustrates the spray-assisted layer-by-layer coating of hydrophobic PpyNW networks between hydrophilic MXene nanosheets for the heterogeneous integration of hierarchically crumpled sensing layers. Morphological characterizations, including (**B**) TEM (inset is the SAED pattern), and (**C**) AFM of the MXene nanosheets (scan area: 5 μm × 5 μm), in conjunction with (**D**) SEM of PpyNWs. Top-view SEM images of PpyNWs and MXene layers with aligned wrinkles and waves formed after releasing the prestretched hydrogel in (**E**) the *y* direction and (**F**) the *x* direction, respectively. The insets show the higher-magnification SEM images of highly entangled PpyNWs and wrinkled MXene nanosheets. (**G**) Cross-sectional SEM image of MXene-PpyNW-VSNP-PAM e-skin. (**H**) Optical images of water droplets on dissimilar composite surfaces and the corresponding contact angles. (**I**) Temperature-dependent FTIR spectra of VSNP-PAM-PpyNW and MXene-PpyNW upon heating from 25° to 200°C. (**J**) Mechanical scratch tests carried out to demonstrate the reinforced adhesion between MXene and hydrogel network by introducing PpyNWs. (**K**) Corresponding optical images of their surface after scratch testing.

sensing material, which has been proven to be a good platform to act as both interconnectors and active elements in e-skin devices (*25*). Colloidal MXene suspensions were prepared using the method described in our previous work (*26*). Figure S6 presents a typical scanning electron microscopy (SEM) image of the single- to a few-layered $Ti_3C_2T_x$ MXene flakes on an anodic aluminum oxide (AAO) substrate. The lateral dimension of the nanosheets is in the range of hundreds of nanometers up to several micrometers. The successful preparation of $Ti_3C_2T_x$ MXene nanosheets can also be confirmed by x-ray diffraction (XRD) based on the shift of the (002) peak to a smaller angle and the greatly weakened peak at 39° (fig. S7). Selected-area electron diffraction (SAED) by transmission electron microscopy (TEM) indicates a typical hexagonal symmetry of MXene (Fig. 3B). The thickness of the flake is determined to be around 1.6 nm according to the atomic force microscopy (AFM) measurement (Fig. 3C), which is in good agreement with the previous report (*13*). The concentrations of the stable suspensions of delaminated MXene nanosheets were further adjusted in the range of 1 to 2 mg/ml for the following device fabrication.

Conductive PpyNWs that serve as hydrophobic intercalants as well as nanobridges were synthesized by a surfactant-assisted soft template approach with cetyltrimethylammonium bromide (CTAB) (*27*). Aqueous dispersions of PpyNWs with a concentration of 1 mg/ml were prepared by probe ultrasonication. Figure 3D shows the hairlike uniform PpyNWs with diameters ranging from 40 to 60 nm. The narrow distribution in diameters ensures the preparation of uniform PpyNW films. Next, a thin continuous layer of PpyNWs was spray-coated onto a prestretched (1000% strain in the *y* direction) VSNP-PAM hydrogel substrate. After releasing the strain, the conductive flexible PpyNWs wrap up together into bunch-like clusters to construct a regularly textured structure with a combination of smooth undulations and sharp ridges, folds, and vertices (Fig. 3E). The PpyNW-VSNP-PAM substrate is then restretched back to 1000% along the *x* direction. Next, the MXene nanosheets are spray-coated onto the prestretched PpyNW-VSNP-PAM substrate. Thereafter, the prestrains in the substrate are relaxed along the *x* direction. During relaxation, thin films of MXene develop aligned wrinkles and delaminated buckles (Fig. 3F). Note that the high degree of crumpling may be the result of vacuum environment inside the SEM chamber. Optical image in fig. S8 provides the surface morphology of orthogonally crumpled MXene-PpyNWs on a hydrated VSNP-PAM for reference. The coating of orthogonally crumpled MXene-PpyNWs was repeated for four cycles to constitute the sensing component for e-skins, unless stated otherwise. Meanwhile, the composite hydrogel composed of MXene nanosheets embedded within the VSNP-PAM hydrogel matrix is also prepared for a control experiment. The mixed composite hydrogel only stayed as a stable colloidal dispersion for half an hour and became irreversibly scrambled, presumably as a result of agglomerated 2D flakes that disrupt the cross-linking points of the VSNP-PAM matrix.

PpyNWs play a crucial role in this heterogeneous integration. On the one hand, they act as hydrophobic intercalation layers (*28*), weakening the interactions between MXene flakes and free water molecules in the hydrogel, and preventing the MXene sheets from randomly sliding with water molecules, self-stacking, and ultimately delaminating from the surface of hydrogel. On the other hand, PpyNWs can be deemed as a double-sided adhesive (*28*) that forms both noncovalent and covalent nanobridges between MXene nanosheets and VSNP-PAM hydrogel networks. At the interface between PpyNWs and VSNP-PAM hydrogels, namely, interface A, covalent topological adhesion (carbon-carbon bond formed via post-polymerization of the AM monomers) (*29*) works collaboratively with both covalent and noncovalent topological entanglement (*30*) and abundant hydrogen bonding helps maintain the structural integrity, as schematically illustrated in fig. S9. Cross-sectional SEM images shown in Fig. 3G and fig. S10 collectively support the notion that PpyNWs can maintain the overall heterostructures over multiple crumpling-unfolding cycles during depositions of both PpyNWs and MXene nanosheets. Meanwhile, the interface between PpyNWs and MXene nanosheets, designated as interface B, is held only by the spatially abundant hydrogen bonding between PpyNW and MXene. The lack of chemical/covalent bonding at interface B enables MXene nanosheets to slide uniformly under extremely large and recurring deformation of e-skin. In addition, the controlled crumpling of MXene-PpyNW layers creates a combination of smooth undulations and/or sharp folds and creases, enabling a Cassie-Baxter–like model and thus displaying an increase of water contact angles in Fig. 3H. Note that the innate hydrophilicity of MXene nanosheets fosters a very strong interaction with water molecules. As a consequence, MXene nanosheets can easily slide and ruinously delaminate along with the migration of free water molecules in VSNP-PAM hydrogels. Therefore, the formation of hierarchical heterostructures of MXene-PpyNW achieved by prestretching and relaxing in conjunction with the intrinsically hydrophobic PpyNWs suppresses the random sliding of MXene nanosheets with free water molecules (*28*). To our knowledge, the combination of stretchability and tunability has not been achieved by existing MXene-hydrogel e-skins.

In situ temperature-dependent Fourier transform infrared (FTIR) spectroscopy was conducted to analyze the hydrogen bonding (Fig. 3I and fig. S11) induced by PpyNWs. For VSNP-PAM-PpyNW composite, the peak between 1600 and 1700 cm^{-1}, which referred to $H_2N{-}C{=}O$ leakage, shifted to higher wave number (from 1683 to 1700 cm^{-1}). Similarly, the $-C{=}O$ band from MXene in MXene-PpyNW spectra also had a blue shift from 1625 to 1646 cm^{-1} after heating. These results indicate the breakage of hydrogen bonding between PpyNWs, VSNP-PAM hydrogel, and MXene nanosheets under heating (*31*). X-ray photoelectron spectroscopy (XPS) also shows the presence of multiple hydrogen bonding (fig. S12 and tables S1 and S2). In addition, the incorporation of PpyNW turns the e-skin to be scratch resistant. Mechanical scratch tests were carried out on the MXene-PpyNW-VSNP-PAM e-skin. As demonstrated in Fig. 3J, stress of 14 mN was applied via a probe to the surface of e-skin placed on a 30° slope. From the optical images, the pure MXene layer is damaged/lost at regions after abrasion by the probe, leaving a large blank area on the surface (Fig. 3K, left). In contrast, the MXene-PpyNW sensing layer remains intact on the VSNP-PAM hydrogel substrate with no loss or slippage (Fig. 3K, right). In parallel, we also compare the adhesions of MXene and MXene-PpyNW sensing layer to the VSNP-PAM hydrogel substrate using 3M tape pull-up tests. As expected, e-skin that comprises pure MXene sensing layer can be easily exfoliated from the VSNP-PAM hydrogel substrate, whereas MXene-PpyNW sensing layers remain firmly attached to and tightly integrated with the VSNP-PAM networks (fig. S13). The demonstration of abrasion resistance and firm adhesion against pull-up tests further underscores the importance of incorporating PpyNWs at various interfaces, establishing a dynamic balance of cross-linking and stepwise sliding of the sensing layers. Such an interfacial adhesion effect has also been reported by Liu *et al.* (*32*), who introduced biomimetic roots under the gold (Au) electrode as an interlocking layer to enhance the adhesion between the polymeric substrate and the electrode layer. As a result, the e-skin maintains stable and continuous conductive pathways under stretching in different

directions and avoids the abrupt enlargement of individual localized fractures (*33*), paving the way for wide working range, superior linearity, and stable electrical properties critical for the e-skin system.

Electromechanical behaviors

Prestretching-and-releasing cycles induce a spring-like morphology of 1D PpyNWs and crumpled patterns of 2D MXene in different directions (Fig. 3, E and F), enabling the stable and uniform expansion of the network. Thus, a reversible stretching in the *x* and *y* directions to 10 to 30 times larger than the original size of the e-skin can be achieved. The figure of merit to evaluate the sensitivity (*S*) of the MXene-PpyNW-VSNP-PAM e-skin is defined as GF = $(R - R_0)/R_0\varepsilon$, where ε is the strain, R_0 is the initial resistance, and *R* represents the real-time resistances under various strains. It can be seen that the relative resistance $(R - R_0)/R_0$ and GF scale linearly when subjected to 800% strains and experienced a slow gradient increase in the strain range beyond 800%, with a maximum GF of 16.9 upon stretching in the *x* direction as well as a GF of 11.2 upon stretching in the *y* direction (Fig. 4A). The capability of discriminating detections and enabling ultrawide sensing range in two axes has not been achieved by state-of-the-art MXene-hydrogel e-skins (table S3). This may stem from the buckling that leads to formation of the two orthogonal buckles of 2D MXene crumples and 1D PpyNWs clusters.

E-skins made of spraying PpyNW and MXene layers on hydrogel substrates with unidirectional prestretching (*x* direction only) were prepared for comparison. Figure S14 reveals the discernible gaps between parallelly aligned crumpled composite films. These localized gaps and associated impaired conduction pathways have an important consequence on the sensing performance. Figure S15 shows the inferior working range of e-skin in the *y* direction (<300%) relative to that of the *x* direction (~1500%). To verify the impact on buckling during the prestretch-and-release cycles of VSNP-PAM hydrogel substrates, both substrates were coated with four cycles of MXene-PpyNW composite layers. Relative electrical resistance as a function of applied strain juxtaposes the distinctively different response. Figure S16 recorded the dissimilar responses for both pre- and nonstretched e-skins. Prestretched e-skin, namely, Y-S, displayed an anisotropic response in the *x* direction over a stable and wide working range. Meanwhile, the electrical resistance response of nonstretched e-skin, namely, N-S, is isotropic and is limited to less than 400% of strain, which is due to the inadequate cross-link of MXene-PpyNW composites with the hydrogel surface, and MXene-PpyNW composites are cluttered and cannot form out-of-plane folds to accommodate strains. When the device is stretched, the sensing active material on the surface undergoes nonuniform strain/stress, which cannot move uniformly with the deformation of hydrogel networks, resulting to locally large cracks (fig. S17), accompanied by large resistance changes.

Next, we draw a comparison between e-skins made with pure 2D MXene nanosheets (M-S) or pure 1D PpyNWs (P-S). Both M-S and

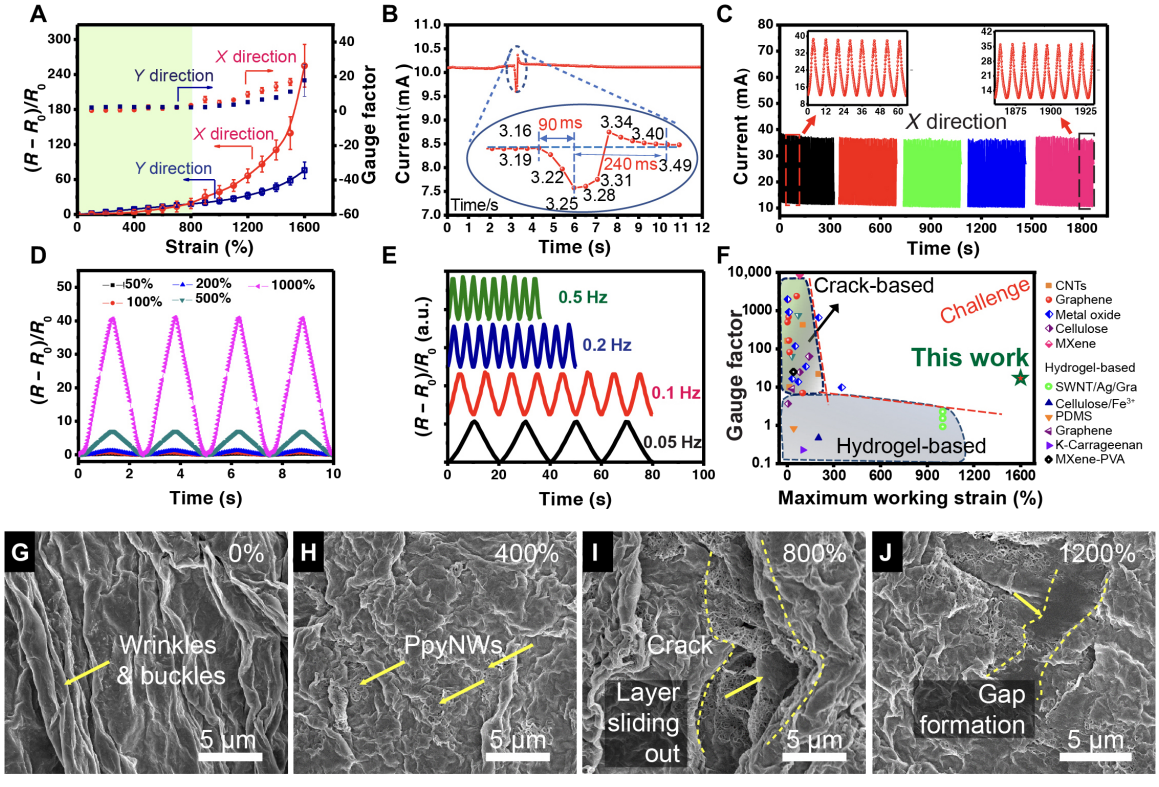

Fig. 4. Electromechanical behaviors and piezoresistive crack propagation sensing mechanism. (**A**) Relative resistance-strain curves and gauge factors of a MXene-PpyNW-VSNP-PAM–based e-skin sensor recorded at *x* and *y* directions, respectively. (**B**) Real time, fast response (~90 ms), and recovery (~240 ms) of the e-skin sensor upon application of a tiny touch. (**C**) Durability test of the e-skin sensor under a strain of 800% at a frequency of 0.12 Hz. The current change curves were recorded after each 1000 cycles, and 45 cycles of data were presented in each record (*x* direction). (**D**) Multicycle tests of relative resistance variation as a function of time (strain frequency, 0.4 Hz) upon stretching to different maximum strains (50, 100, 200, 500, and 1000%). (**E**) Relative resistance response of the e-skin sensor at different frequencies under a strain of 1000%. a.u., arbitrary units. (**F**) Gauge factor as a function of a maximum reliable working range of the present e-skin sensor along with recently reported sensors adapted from (*17*, *35*, *36*). (**G** to **J**) Surface SEM images of MXene-PpyNW-VSNP-PAM e-skin sensor taken at various stretching states: (G) 0%, (H) 400%, (I) 800%, and (J) 1200%.

P-S were treated with prestretch-and-release cycles before stretching tests. In the case of M-S, MXene nanosheets are hydrophilic in nature, which, in turn, strongly interact with the water molecules on the surface of VSNP-PAM hydrogels. These MXene nanosheets thus tend to slide over from each other and ultimately delaminate from the VSNP-PAM hydrogels under strain. The result is the disruption of percolation networks and failed external electrode connections. It is worth noting that, similar to the samples prepared without prestretching (N-S), resistance response of P-S is also isotropic and cannot be differentiated in multiple directions. As indicated in fig. S18, the relative resistance, $(R - R_0)/R_0$, of P-S increases slowly and steadily in the strain range up to 1500%, closely resembling the response of Y-S. It is intriguing to note the difference in response of sensitivity of P-S and Y-S. Achieving the high sensitivity of strain sensor requires active sensing components to undergo the considerable structural deformation at the inception of applied strain, whereas high stretchability hinges on the ability to maintain structural connection or preserve morphological integrity for active sensing components upon large deformation. Therefore, the combination of face-to-face oriented stacking configuration and 2D structure of inherently stiff MXene nanosheets, high aspect ratio, and spatially abundant and retractable conductive pathways of 1D PpyNWs and buckling-induced self-organized hierarchical structures has made these exceptional mechanical and sensing properties possible. Figure S19 features the cross-sectional SEM image of P-S and Y-S.

The heterogeneously integrated e-skin also shows an excellent combination of response and recovery times to external stimuli. It is known that hydrogels typically take a long time (>1 s) or even fail to recover because of the toughness and hysteresis correlation (*34*), making it difficult to fulfill the requirements of full-range human physical activities. The reaction time of healthy people is usually between 100 and 300 ms. As shown in Fig. 4B, our heterogeneously integrated e-skin enables very fast response (~90 ms) and recovery (~240 ms), exceeding most of the reported hydrogel-based strain sensors (*17*). Moreover, Fig. 4C shows that the MXene-PpyNW-VSNP-PAM e-skin exhibits a high durability under a cyclic strain of 0%–800%–0% in the x direction at a frequency of 0.12 Hz and a stage moving speed of 36 mm s^{-1}. The negligible current changes indicate that the e-skin sensor exhibits high repeatability, stability, and durability even under broad working range, making it more suitable for practical applications than most of the reported MXene hydrogels.

We further investigate the dynamic electromechanical properties of the e-skin (Fig. 4, D and E). To this end, an integrated testing platform composed of stretchable station, force gauge, and a standard semiconductor parametric tester (Keithley 4200) was assembled. The cycling and dynamic force measurements were performed via a motorized moving stage (z axis). The speed, distance, and cycles of movement are modulated by the grating embedded in the stretchable stage. Therefore, the $\Delta L/L_0$ (ΔL: change of length, L_0: original length) of the device can also be calculated through the values recorded by the grating. The variation in relative resistance upon stretching (x direction) to maximum strains of 50, 100, 200, 500, and 1000% was measured to be 0.25, 0.64, 1.23, 6.97, and 40.54, respectively (Fig. 4D), and these results are in good agreement with those shown in Fig. 4A. Figure 4E shows the frequency response and output signals of the as-prepared stretchable e-skin. It can be seen that the electrical responses of the sensors display stable durability with 1000% strain at frequencies ranging from 0.05 to 0.25 Hz. As the frequency increases, the peak variations of the relative resistance are almost the same. This can be attributed to the proper adhesion and dynamic interfacial linkages between MXene, PpyNWs, and VSNP-PAM networks. Furthermore, the recoverability and frequency response of the e-skin with more spray-coating cycles of PpyNW and MXene (six cycles) were investigated (fig. S20, A to D). The resistance waves are almost the same as the input tension waves under a dynamic strain of 1000% with different frequencies of 0.05, 0.1, 0.2, and 0.25 Hz when the stage moving speed is 1.5, 3.0, 6.0, and 7 mm s^{-1}, respectively. Even when the speed reaches 7 mm s^{-1}, the output resistance signals remained stable with a negligible hysteresis (fig. S20D). For comparison, we have summarized a number of recently reported stretchable sensing devices, including crack-based sensors (*35*) and hydrogel-based sensors fabricated with conductive fillers (*17*, *36*). They exhibit narrow sensing ranges (<100%) and/or low sensitivities (<10) (Fig. 4F).

The sensing mechanism of the MXene-PpyNW-VSNP-PAM e-skin sensor was explored by surface SEM images as shown in Fig. 4 (G to J). In the initial stages before stretching (Fig. 4G), the hydrogel shows an aligned "wavy" morphology because of the prestretch coating and release processes used during fabrication. The 2D MXene nanosheets are closely attached onto the surface of hydrogel networks through multiple linkages with the 1D PpyNW layers. Within a relatively low strain region (<400%), the waves of the film are gradually flattened by external tension in the x direction, exposing a small amount of PpyNWs under the MXene layers (Fig. 4H). This observation implies that only minor microcracks or gaps appear on the MXene layers. With increasing strain, cracks grow gradually and propagate throughout the entire composite film (Fig. 4I). The synergistic effect of polymer chain stretching, hydrogen bonding, topological entanglement, hydrophobic intercalation, and gradient sliding of sensing layers in the heterostructures enables the MXene-PpyNW-VSNP-PAM e-skin to accommodate applied tension gradients over very large strains, resulting in great mitigation on crack propagation. Therefore, the e-skin can exhibit stable continuous current changes under larger strains owing to the interconnected electron pathways. With further increased strain, conductivity was reduced rapidly as a result of less sensing layer interconnection (Fig. 4J). This piezoresistive crack propagation sensing mechanism and the wavy morphology dominate the stretching process and ensure high sensitivity and ultralarge working strain range.

Capacitive tactile behaviors

Besides tension sensing capabilities, our e-skin is capable of discerning the approaching objects or gentle tactile-based inputs (in the z direction). Semitransparent and compressive parallel plate capacitors were fabricated using two strips of MXene-PpyNW-VSNP-PAM stretchable e-skins laminated with the patterned surfaces placed back to back. Elastic tape (VHB 4905, 3M Inc.) was used for dielectrics and encapsulation (Fig. 5A). Various capacitances (Fig. 5B) are defined as sensor capacitances (C_{total}), plate electrode capacitance (C_p), fringing capacitance in the VHB overlay (C_{f1}), and fringing capacitance through the medium directly above the sensor (C_{f2}). In theory, the capacitance change in the touch detection originates from the disturbance of the fringing electric field and the dimension change of the dielectric (*37*). When a finger of one person approaches the e-skin attached to the forearm of another person,

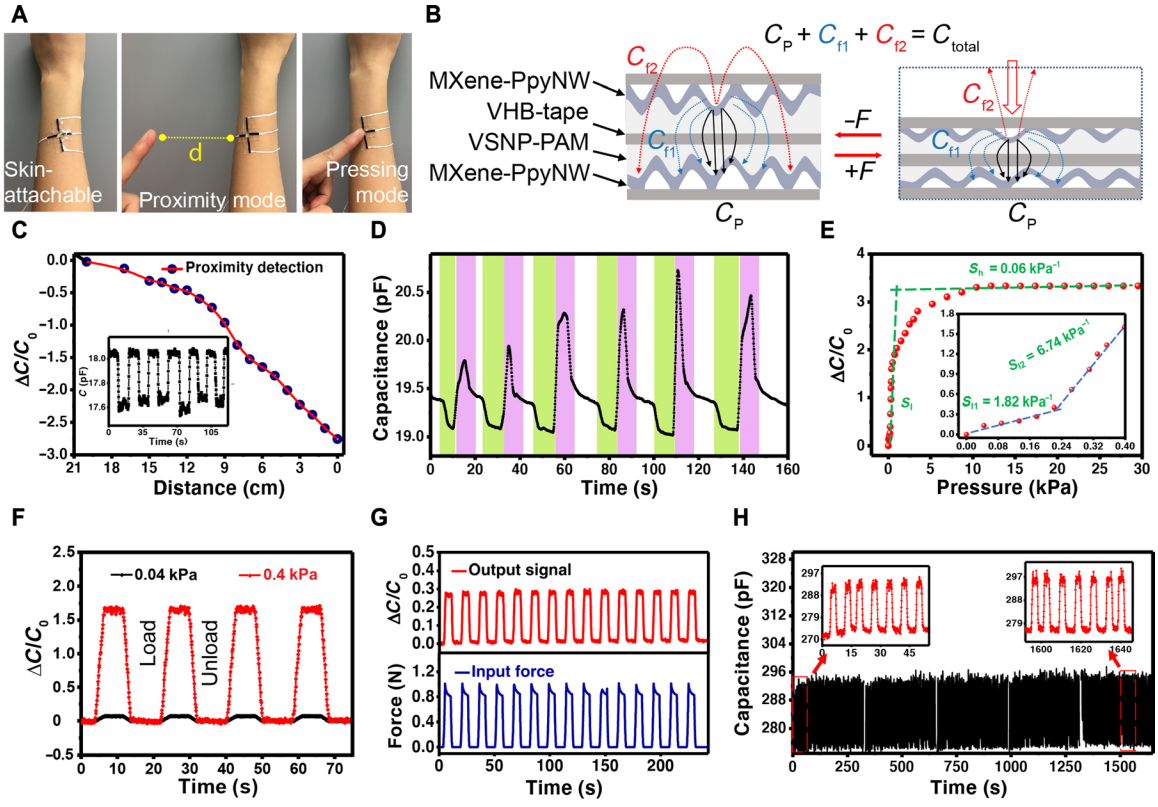

Fig. 5. Capacitive tactile behaviors and mechanisms of e-skin. (**A**) Skin-attachable MXene-PpyNW-VSNP-PAM–based e-skin placed on the forearm. Investigation proceeds with a proximity mode followed by a pressing mode via a finger of the other person. Photo credit: Yichen Cai and Jie Shen, KAUST. (**B**) Schematic illustration shows the capacitance mechanism of a parallel plate capacitor. (**C**) Relative capacitance change decreases when a finger approaches the e-skin. The inset further demonstrates the continuous changes in capacitance when a finger repeatedly approached upon and removed away from the e-skin sensor. (**D**) Cyclic tests of capacitance changes from a finger approaching the e-skin cyclically (green, from a distance of approximately 2 cm), touching (pink), and finally moving away from it (white). (**E**) Relative capacitance changes of the e-skin in response to various pressures. (**F**) Capacitance changes of the e-skin constructed with two tensile sensors for detection of a tiny pressure (40 Pa) and relatively large pressure (400 Pa). (**G**) Time retention curve of the change in response to capacitance and force. (**H**) Tactile durability test of the e-skin sensor under a pressure of 1.0 kPa at a frequency of 0.13 Hz. The current change curves were recorded after each 1000 cycles, and 45 cycles of data were presented in each record.

the fringing electric field is partially intercepted and shunted to the ground by the finger, leading to a decrease in capacitance (Fig. 5C). The relative capacitance changes with respect to the distance of an approaching finger, and the capacitance decreases rapidly and linearly when the distance is less than 10 cm (Fig. 5C). The inset demonstrates the continuous changes in capacitance when a finger repeatedly approached upon and removed away from the e-skin sensor. In addition, we also made a comparison between a finger approaching and removing away from the e-skin with and without an ungrounded insulating object placed aside (fig. S21). It becomes apparent that the capacitive mechanism remains effective despite the interference of an insulating object in close proximity. Figure 5D shows that the capacitance changes according to a finger approaching (green, decrease), touching (pink, increase), and moving away (white, recovery to original value) from the e-skin. The decreased capacitance emanates from the disturbance of the fringing electric field coming from the finger approaching, while the increase comes from the dimension change of the dielectric from the gentle pressing. Asymmetric peaks stem from the subtle nuance of approaching speeds, angles, and applied pressures of an object's finger at each cycle. These data indicate that noncontact (proximity) and contact (touch) sensing mode coexist, holding tantalize prospects for prosthesis/robots with real sensations. Figure S22 illustrates the capacitive working mechanisms of tactile sensing.

Changes in capacitance caused by the deformation pressure were further investigated (Fig. 5E). The pressure sensitivity S is defined as $\Delta C/C_0\Delta P$, where ΔC is the change of capacitance, C_0 is the original capacitance, and ΔP is the applied pressure change. Sensitivities of 1.82 kPa^{-1} (<0.2 kPa range) and 6.74 kPa^{-1} (0.2 to 0.4 kPa range) are observed, which are larger than previously reported values (*38*, *39*). A subtle pressure vibration of gas flows can be detected (movie S1). Figure 5F presents capacitance versus time for four cycles of applied pressure (40 and 400 Pa) using an electrically insulating tip to apply the load for testing. Each curve is stable and continuous without obvious signal attenuation under each loading and unloading cycle. The output current capacitance changes are compared with the dynamic pressure inputs, where 5 s of static pressure was applied for each cycle (Fig. 5G). The capacitance waves are almost identical to the input pressure waves, indicating the excellent response of the e-skin when subjected to externally exerted pressures. In addition, the as-prepared MXene-PpyNW-VSNP-PAM e-skins are able to reliably identify complex patterns and distinguish handwriting words repeatably through changes in capacitance waveforms that correspond to the tip of a stylus press. Repeated and real-time capacitance changes can be seen

when an object writes "KAUST" on the sensor (movie S2), providing promise for applications in electronic signatures and human/machine interactions. Similarly, our piezoresistive e-skin was also used for the recognition of handwriting letters: "C," "O," "L," and "I" characteristic with similar strokes. As shown in fig. S23, each letter corresponds to a distinctive output waveform on the basis of the different strength, direction, and speed of their corresponding strokes. As demonstrated in the recent work (*40*), integrating e-skins with neuromorphic computing and machine learning holds tantalizing prospect to potentially achieve the distinguishing recognition of words and output them to an electronic screen.

The durability of the e-skin sensor was also evaluated under a cyclic pressure of 0 Pa–1000 Pa–0 Pa at a frequency of 0.13 Hz (Fig. 5H). The capacitance curves indicate a negligible increase after 5000 testing cycles, presenting high recovery, stability, and durability. The sensing capability for other multimodal stimuli, such as temperature and light radiation variation, enables more complex and contextual tasks (figs. S24 and S25). Owing to the very high extinction coefficient of MXene, the MXene-PpyNW-VSNP-PAM e-skin performs well as a photothermal sensor (fig. S25). In addition, the sensing performance of the e-skin under simultaneously mixed stimulation is shown in fig. S26. The e-skin, which is constructed by laminating heterostructure networks, showed a very subtle dependence of capacitance on temperature under increasing pressure. Meanwhile, the change in resistance corresponds in a distinguishable pattern to the incremental changes only in temperatures over the range of 0 to 0.25 kPa. Such an anisotropic yet regular pattern in response to temperature changes facilitates the simultaneous sensory of multimodal environmental stimuli, currently unachievable in state-of-the-art MXene-hydrogel sensors.

Wireless transmission and remote monitoring

Sensing responses of e-skin can be recorded, analyzed, and then uploaded to the cloud by a wireless transmitter and an analyzer, which can be synchronized to the user interface via a wireless Wi-Fi network. The microcontroller unit (MCU) is mainly composed of microprocessors, Wi-Fi module, Bluetooth, and light-emitting diode (LED). We can use the Wi-Fi module to add networking capabilities to the existing devices or to build separate network controllers. The powerful on-chip processing and storage capabilities of MCU enable the integration of e-skin through the general-purpose input/output port and then receive and send digital/analog signals for LED or other modules. All modules were installed on a mounting plate for convenience, with general-purpose output connected with LEDs to make the debug process. Upon testing, the resistance and capacitance changes are collected and processed by the analog-to-digital converter in the processors (Fig. 6A). Therefore, sensing responses of e-skin can be recorded, analyzed, uploaded to the cloud, and

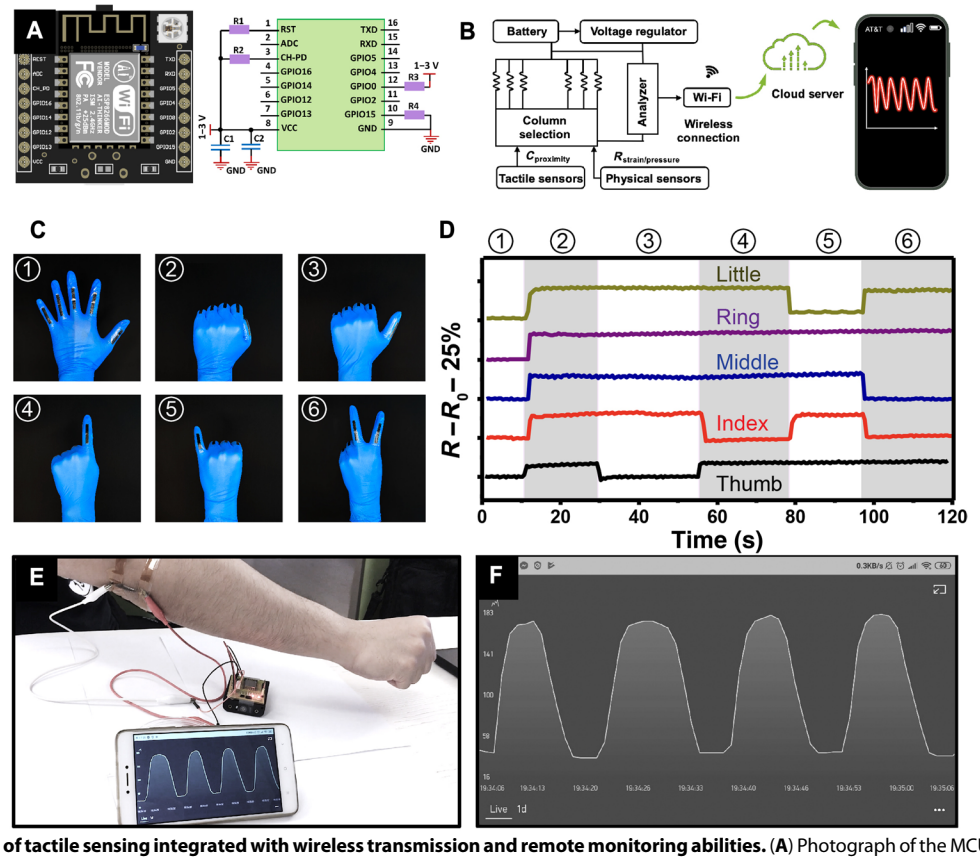

Fig. 6. An e-skin capable of tactile sensing integrated with wireless transmission and remote monitoring abilities. (**A**) Photograph of the MCU ESP8266 and the circuit connection settings with devices. Photo credit: Yichen Cai and Jie Shen, KAUST. (**B**) Circuit scheme showing the signal transduction, processing, and wireless transmission from the e-skin sensors to the iPhone 11 Pro Max. (**C**) Photographs of a "data glove" mounted with the assembled e-skin sensors to perform a series of gestures. Photo credit: Vincent Tung, KAUST. (**D**) Relative resistance changes of e-skins in response to six different gestures in (C). (**E**) Photograph of a remote and wireless (Wi-Fi) monitoring system. (**F**) Snapshot of the sensing responses received wirelessly by a smart phone under bending cycles of the elbow joint. Photo credit: Yichen Cai and Jie Shen, KAUST.

then synchronized to the user interface via a wireless Wi-Fi network (Fig. 6B).

The stretchable and compressible e-skin system provides multidimensional sensing capabilities, which can be used for monitoring a full range of human motion from tiny vibrations caused by blood pressure to large limb deformations and long-term exercises. Figure S27 presents data obtained from a flexible e-skin mounted on an individual's wrist. Characteristic arterial waveform peaks including percussion (*P*), tidal (*T*), and diastolic (*D*) peaks are observed when devices are operated at an applied voltage of 1 V. For large limb deformations, a data glove assembled with five independent strip e-skin sensors can detect the motion of each finger individually and precisely (Fig. 6, C and D). Compared to conventional data glove systems based on optical fibers or metal strain gauges, our data glove is thinner, lighter, and easier to integrate while simultaneously offering an ultrabroad working range than the metal strain gauge device. For the reversible process of bending and straightening the elbow joint, our stretchable sensory system displays repeated and real-time resistance changes (Fig. 6E and movie S3), which can be used as a wirelessly remote interactive device to facilitate fine-motion control in robotics and virtual reality. In addition, the capability to provide continuous physiological data, such as tracking functional movements, workload, and biovital markers, permits the development of treatment plans and athlete-training programs to potentially alleviate injuries (fig. S28). Detecting the facial microexpression tests is also shown in fig. S29.

Moreover, a smart artificial e-skin platform is assembled to detect and map distribution of various tactile signals and spatial pressures (fig. S30). The versatility of the spray-assisted heterogeneous integration can be further extended by replacing the rigid and less-than-flexible metal interconnect with the soft, flexible, and stretchable MXene-PpyNW composites. A fully flexible electrode array using MXene-PpyNW as interconnecting components is demonstrated via a shadow mask–assisted spray coating. The detailed designs and dimensions of the shadow mask for both electrodes and interconnects are included in fig. S31 (A and B). Arrays of sensing components can be deposited through the shadow mask with the squared openings (fig. S31C). The resultant electrode array can be conformally attached to a thumb as showcased in fig. S32. The results hold promise for using an all MXene-PpyNW material system for a scalable production of e-skin.

DISCUSSION

Blurring the line between artificial and biological skins requires the convergence of advances in mechanical durability, conformality, stretchability, and the ability to measure a diversity of complicated sensations. Investigating isolated components within the e-skin is no longer sufficient to tackle these engineering challenges. To this end, we unveil a heterogeneous integration that synergistically combines insights from both intermolecular forces and mechanical engineering to circumvent inherent obstacles at the interfaces between individual components within the e-skin. The VSNP-engineered PAM hydrogels first overcome the correlation between toughness and hysteresis, thus establishing the mechanically compliant and robust basis for e-skins. Next, the approach to control reversible crumpling and unfolding of the VSNP-PAM hydrogels yields hierarchically structured and orthogonally aligned morphology of MXene-PpyNW sensing layer that delivers the tunable sensing capabilities, an extraordinary working range (0 to 2800%), ultrafast responsiveness (~90 ms), outstanding resilience (~240 ms), good linearity (0 to 800%), and excellent reproducibility (>5000 cycles). These exceptional properties are made possible by the dynamic interfacial linking that hinges on immobilized MXene nanosheets while enhancing the interfacial adhesion. In parallel, the heterogeneously integrated e-skin is capable of detecting, quantifying, and remotely monitoring stretching motions in multiple dimensions, tactile pressure (40 Pa to 30 kPa), proximity sensing (from a distance of ~20 cm), and variations in temperature and light. Last, this general platform, which is directed by the heterogeneous integration of 2D sheets and 1D nanowires on the prestrained VSNP-PAM hydrogel substrate, is not limited to the MXene-PpyNW combination reported here. Instead, it could be generalized for including a wide variety of MXene families, both semiconducting and metallic transition metal dichalcogenides and inorganic nanowires, toward the development of e-skin with tailored material properties and multifunctional capabilities.

MATERIALS AND METHODS

Preparation of VSNP-PAM hydrogel

The synthesis of VSNP-PAM hydrogel is adopted from the reported method (*41*). Briefly, vinyltriethoxysilane (0.633 g; Sigma-Aldrich) was added into DI-H_2O (5 ml), followed by vigorous stirring for 12 hours. After the disappearance of oil-like droplets, an emulsion of VSNPs was obtained. Emulsion (1 ml) was diluted with DI-H_2O to 10 ml. Afterward, diluted VSNP emulsion (95.2 μl), AM monomer (1.2 g; Sigma-Aldrich), and ammonium persulfate (0.005 g; Sigma-Aldrich) were added into 18 ml of DI-H_2O. During the magnetic stirring, the resultant solution was degassed with nitrogen bubbles to remove the dissolved oxygen. The solution was then poured into a mold and sealed in a water bath (40°C) for free-radical polymerization lasting 20 hours. Finally, the obtained polymer networks were transferred to a mixed solution of DI-H_2O and glycerol in a certain ratio (1:4) for 12 hours to remove unreacted monomers and exchange the solvents.

Synthesis of $Ti_3C_2T_x$ MXene

The preparation of $Ti_3C_2T_x$ aqueous dispersions is based on our previous work in which the Ti_3AlC_2 powder (~50 μm) is chemically exfoliated by HCl + LiF etchant (*26*). The Ti_3AlC_2 powder (1 g; 11 Technology Co. Ltd.) was slowly added into a mixture of 0.666 g of lithium fluoride (LiF; Sigma-Aldrich) in 10 ml of 9 M hydrochloric acid (HCl; Sigma-Aldrich), followed by stirring at 35°C for 24 hours. The acidic suspension was washed with ethanol and centrifuged several times until pH ≥ 6 is reached. The sediment was collected, followed by adding 50 ml of DI water. After sonication and subsequent centrifugation at 3500 rpm, a stable colloidal suspension of delaminated $Ti_3C_2T_x$ MXene (d-$Ti_3C_2T_x$) was obtained. MXene membranes were formed by filtering specific amounts of colloidal solution (3 to 5 ml) through AAO membranes, followed by drying at room temperature under vacuum. Then, the concentration of d-$Ti_3C_2T_x$ suspension was calculated by mass changes of AAO membranes and the volume of filtered dispersions. By further dilution with DI-H_2O, the concentration of the $Ti_3C_2T_x$ MXene suspension was regulated in the range of 0.5 to 2 mg/ml.

Synthesis of PpyNWs

PpyNWs were prepared by adding 0.91 g of the surfactant, CTAB (Sigma-Aldrich), into a solution consisting of 0.3 ml of pyrrole monomer

dissolved in 125 ml of 0.2 M HCl. Then, the mixture was stirred for 2 hours at 0° to 5°C, followed by dropwise addition of the oxidizing agent ammonium persulfate (Sigma-Aldrich) dissolved in 10 ml of 0.2 M HCl solution. Next, polymerization was carried out for 24 hours under continuous stirring at 0° to 5°C. Last, the black precipitate was filtered and washed with copious amounts of DI-H_2O and dried at 50°C vacuum. To prepare the uniform dispersions of PpyNWs with special concentration (1 mg/ml), ultrasonic probe was used to ensure the uniform dispersion.

Construction of MXene-PpyNW-VSNP-PAM e-skin sensors

The procedures of fabricating e-skin sensors are as follows: Soft VSNP-PAM hydrogel elastomer was first cut into a certain size and was prestretched to 1000% in the *y* direction. Then, the first layer of PpyNWs was spray-coated on the hydrogel surface, followed by drying with a nitrogen flow. After releasing the strain in the *y* direction, PpyNW-VSNP-PAM was again prestretched to 1000% in the *x* direction and spray-coated with d-$Ti_3C_2T_x$ MXene layers. In this manner, the layer-by-layer assembly was used for at least four cycles to construct mechanically robust weaving networks consisting of alternating MXene and PpyNWs layers. It is noted that MXene-PpyNW-VSNP-PAM can be directly used as a tension sensor with two external electrodes. For capacitive tactile sensors, a stretchable dielectric layer (VHB 4905, 3M) was sandwiched between two MXene-PpyNW-VSNP-PAM layers, which were laminated back to back and connected to two electrodes. After that, the whole device was sealed with VHB tapes.

Matrix panel fabrication

MXene-PpyNW-VSNP-PAM networks with each sensing pixel element (4 mm × 4 mm) extended to additional contact pads, and 25 pixels (5 pixel × 5 pixel arrays) form the basis of the integrated capacitive sensing units. The liquid PDMS was poured onto the matrix panel after the fabrication of top electrode arrays followed by curing at room temperature for 48 hours. This PDMS layer helps passivate and protect the sensing panel and fix electrodes. Note that every sensing pixel element and electrode was isolated to avoid the interference of signals from adjacent sensing pixel elements. The fully flexible electrode array using MXene-PpyNW as interconnecting components was fabricated via a shadow mask–assisted spray coating.

Characterization and measurements

The morphology was characterized by field-emission SEM (Magellan XHR 400L, FEI, USA) and TEM (Titan 80-300 ST, FEI, Thermo Fisher Scientific) with an accelerating voltage of 300 kV. XRD patterns were measured with D8 Advance X-ray Diffractometer (Bruker, Germany). To characterize the hydrogen bonding between MXene, hydrogel, and polypyrrole, FTIR (AVATAR-FT-IR-360, Thermo Nicolet, USA) and XPS Thermo (ESCALAB 250, USA) with a monochromatized AlKa radiation (1486.6 eV) were used. Nicolet 6700 was integrated for the temperature-dependent FTIR measurement. The samples were placed into a vacuum cell with a KBr window in tandem with in situ programmable heating and cooling pool. Next, temperature-dependent FTIR spectra were collected upon heating from 25° to 200°C. All the FTIR spectra were gathered by 64 scans with a resolution of 4 cm^{-1} to obtain a good signal-to-noise ratio. Mechanical properties were applied and ascertained by instruments composed of stretchable and compressive station (ESM303), force gauge (M7-2, Mark-10), and a PC. The piezoresistive and capacitive properties of all samples were concurrently measured with a standard semiconductor parametric tester (Keithley 4200). The response time and recovery time of e-skin sensor were tested by gentle touch with a finger.

SUPPLEMENTARY MATERIALS

Supplementary material for this article is available at http://advances.sciencemag.org/cgi/content/full/6/48/eabb5367/DC1

REFERENCES AND NOTES

1. S. Wang, J. Xu, W. Wang, G.-J. N. Wang, R. Rastak, F. Molina-Lopez, J. W. Chung, S. Niu, V. R. Feig, J. Lopez, T. Lei, S.-K. Kwon, Y. Kim, A. M. Foudeh, A. Ehrlich, A. Gasperini, Y. Yun, B. Murmann, J. B.-H. Tok, Z. Bao, Skin electronics from scalable fabrication of an intrinsically stretchable transistor array. *Nature* **555**, 83–88 (2018).
2. C. Larson, B. Peele, S. Li, S. Robinson, M. Totaro, L. Beccai, B. Mazzolai, R. Shepherd, Highly stretchable electroluminescent skin for optical signaling and tactile sensing. *Science* **351**, 1071–1074 (2016).
3. W. Gao, S. Emaminejad, H. Y. Y. Nyein, S. Challa, K. Chen, A. Peck, H. M. Fahad, H. Ota, H. Shiraki, D. Kiriya, D.-H. Lien, G. A. Brooks, R. W. Davis, A. Javey, Fully integrated wearable sensor arrays for multiplexed in situ perspiration analysis. *Nature* **529**, 509–514 (2016).
4. M. A. McEvoy, N. Correll, Materials that couple sensing, actuation, computation, and communication. *Science* **347**, 1261689 (2015).
5. C.-C. Kim, H.-H. Lee, K. H. Oh, J.-Y. Sun, Highly stretchable, transparent ionic touch panel. *Science* **353**, 682–687 (2016).
6. H. Yuk, T. Zhang, G. A. Parada, X. Liu, X. Zhao, Skin-inspired hydrogel–elastomer hybrids with robust interfaces and functional microstructures. *Nat.Commun.* **7**, 12028 (2016).
7. Z. Zhou, J. Liu, X. Zhang, D. Tian, Z. Zhan, C. Lu, Ultrathin MXene/calcium alginate aerogel film for high-performance electromagnetic interference shielding. *Adv. Mater. Interfaces* **6**, 1802040 (2019).
8. L.-X. Liu, W. Chen, H.-B. Zhang, Q.-W. Wang, F. Guan, Z.-Z. Yu, Flexible and multifunctional silk textiles with biomimetic leaf-like MXene/silver nanowire nanostructures for electromagnetic interference shielding, humidity monitoring, and self-derived hydrophobicity. *Adv. Funct. Mater.* **29**, 1905197 (2019).
9. X. Tang, D. Zhou, P. Li, X. Guo, B. Sun, H. Liu, K. Yan, Y. Gogotsi, G. Wang, MXene-based dendrite-free potassium metal batteries. *Adv. Mater.* **32**, 1906739 (2020).
10. J. Yang, W. Bao, P. Jaumaux, S. Zhang, C. Wang, G. Wang, MXene-based composites: Synthesis and applications in rechargeable batteries and supercapacitors. *Adv. Mater. Interfaces* **6**, 1802004 (2019).
11. J. Sun, W. Kong, Z. Jin, Y. Han, L. Ma, X. Ding, Y. Niu, Y. Xu, Recent advances of MXene as promising catalysts for electrochemical nitrogen reduction reaction. *Chinese Chem. Lett.* **31**, 953–960 (2020).
12. G. Monastyreckis, L. Mishnaevsky Jr., C. Hatter, A. Aniskevich, Y. Gogotsi, D. Zeleniakiene, Micromechanical modeling of MXene-polymer composites. *Carbon* **162**, 402–409 (2020).
13. A. Lipatov, H. Lu, M. Alhabeb, B. Anasori, A. Gruverman, Y. Gogotsi, A. Sinitskii, Elastic properties of 2D $Ti_3C_2T_x$ MXene monolayers and bilayers. *Sci. Adv.* **4**, 0491 (2018).
14. R. Li, L. Zhang, L. Shi, P. Wang, MXene Ti_3C_2: An effective 2D light-to-heat conversion material. *ACS Nano* **11**, 3752–3759 (2017).
15. K. Hantanasirisakul, Y. Gogotsi, Electronic and optical properties of 2D transition metal carbides and nitrides (MXenes). *Adv. Mater.* **30**, 1804779 (2018).
16. H. Liao, X. Guo, P. Wan, G. Yu, Conductive MXene nanocomposite organohydrogel for flexible, healable, low-temperature tolerant strain sensors. *Adv. Funct. Mater.* **29**, 1904507 (2019).
17. Y.-Z. Zhang, K. H. Lee, D. H. Anjum, R. Sougrat, Q. Jiang, H. Kim, H. N. Alshareef, MXenes stretch hydrogel sensor performance to new limits. *Sci. Adv.* **4**, eaat0098 (2018).
18. M. Wang, Y. Chen, R. Khan, H. Liu, C. Chen, T. Chen, R. Zhang, H. Li, A fast self-healing and conductive nanocomposite hydrogel as soft strain sensor. *Colloids Surf. A Physicochem. Eng. Asp.* **567**, 139–149 (2019).
19. G. Cai, J. Wang, K. Qian, J. Chen, S. Li, P. S. Lee, Extremely stretchable strain sensors based on conductive self-healing dynamic cross-links hydrogels for human-motion detection. *Adv. Sci.* **4**, 1600190 (2017).
20. X. Jiang, T. Jiang, X. Zhang, H. Dai, The plasticizing effect of calcium nitrate on poly(vinyl alcohol). *Polym. Eng. Sci.* **53**, 1181–1186 (2013).
21. Z. Wang, C. Xiang, X. Yao, P. Le Floch, J. Mendez, Z. Suo, Stretchable materials of high toughness and low hysteresis. *Proc. Natl. Acad. Sci. U.S.A.* **116**, 5967–5972 (2019).
22. C. H. Yang, B. Chen, J. Zhou, Y. M. Chen, Z. Suo, Electroluminescence of giant stretchability. *Adv. Mater.* **28**, 4480–4484 (2016).
23. Z. Jiang, B. Diggle, I. C. Shackleford, L. A. Connal, Tough, self-healing hydrogels capable of ultrafast shape changing. *Adv. Mater.* **31**, 1904056 (2019).
24. G. Lake, A. Thomas, The strength of highly elastic materials. *Proc. R. Soc. Lond. A* **300**, 108–119 (1967).
25. Y. Ma, N. Liu, L. Li, X. Hu, Z. Zou, J. Wang, S. Luo, Y. Gao, A highly flexible and sensitive piezoresistive sensor based on MXene with greatly changed interlayer distances. *Nat. Commun.* **8**, 1207 (2017).

26. Y. Cai, J. Shen, G. Ge, Y. Zhang, W. Jin, W. Huang, J. Shao, J. Yang, X. Dong, Stretchable $Ti_3C_2T_x$ MXene/carbon nanotube composite based strain sensor with ultrahigh sensitivity and tunable sensing range. *ACS Nano* **12**, 56–62 (2018).
27. J. Fang, P. Li, X. Lu, L. Fang, X. Lü, F. Ren, A strong, tough, and osteoconductive hydroxyapatite mineralized polyacrylamide/dextran hydrogel for bone tissue regeneration. *Acta Biomater.* **88**, 503–513 (2019).
28. H. Yuk, C. E. Varela, C. S. Nabzdyk, X. Mao, R. F. Padera, E. T. Roche, X. Zhao, Dry double-sided tape for adhesion of wet tissues and devices. *Nature* **575**, 169–174 (2019).
29. J. Steck, J. Yang, Z. Suo, Covalent topological adhesion. *ACS Macro Lett.* **8**, 754–758 (2019).
30. J. Yang, R. Bai, B. Chen, Z. Suo, Hydrogel adhesion: A supramolecular synergy of chemistry, topology, and mechanics. *Adv. Funct. Mater.* **30**, 1901693 (2019).
31. J. Cao, C. Lu, J. Zhuang, M. Liu, X. Zhang, Y. Yu, Q. Tao, Multiple hydrogen bonding enables the self-healing of sensors for human–machine interactions. *Angew. Chem. Int. Ed.* **56**, 8795–8800 (2017).
32. Z. Liu, X. Wang, D. Qi, C. Xu, J. Yu, Y. Liu, Y. Jiang, B. Liedberg, X. Chen, High-adhesion stretchable electrodes based on nanopile interlocking. *Adv. Mater.* **29**, 1603382 (2017).
33. S. Huang, Y. Liu, Y. Zhao, Z. Ren, C. F. Guo, Flexible electronics: Stretchable electrodes and their future. *Adv. Funct. Mater.* **29**, 1805924 (2019).
34. J.-Y. Sun, X. Zhao, W. R. Illeperuma, O. Chaudhuri, K. H. Oh, D. J. Mooney, J. J. Vlassak, Z. Suo, Highly stretchable and tough hydrogels. *Nature* **489**, 133–136 (2012).
35. X. Shi, H. Wang, X. Xie, Q. Xue, J. Zhang, S. Kang, C. Wang, J. Liang, Y. Chen, Bioinspired ultrasensitive and stretchable MXene-based strain sensor via nacre-mimetic microscale "brick-and-mortar" architecture. *ACS Nano* **13**, 649–659 (2018).
36. K. Tian, J. Bae, S. E. Bakarich, C. Yang, R. D. Gately, G. M. Spinks, M. in het Panhuis, Z. Suo, J. J. Vlassak, 3D printing of transparent and conductive heterogeneous hydrogel–elastomer systems. *Adv. Mater.* **29**, 1604827 (2017).
37. S. Y. Kim, S. Park, H. W. Park, D. H. Park, Y. Jeong, D. H. Kim, Highly sensitive and multimodal all-carbon skin sensors capable of simultaneously detecting tactile and biological stimuli. *Adv. Mater.* **27**, 4178–4185 (2015).
38. X. Wang, Y. Gu, Z. Xiong, Z. Cui, T. Zhang, Silk-molded flexible, ultrasensitive, and highly stable electronic skin for monitoring human physiological signals. *Adv. Mater.* **26**, 1336–1342 (2014).
39. S. Park, H. Kim, M. Vosgueritchian, S. Cheon, H. Kim, J. H. Koo, T. R. Kim, S. Lee, G. Schwartz, H. Chang, Z. Bao, Stretchable energy-harvesting tactile electronic skin capable of differentiating multiple mechanical stimuli modes. *Adv. Mater.* **26**, 7324–7332 (2014).
40. M. Wang, Z. Yan, T. Wang, P. Cai, S. Gao, Y. Zeng, C. Wan, H. Wang, L. Pan, J. Yu, S. Pan, K. He, J. Lu, X. Chen, Gesture recognition using a bioinspired learning architecture that integrates visual data with somatosensory data from stretchable sensors. *Nat. Electron.* **3**, 563–570 (2020).
41. Y. Huang, M. Zhong, Y. Huang, M. Zhu, Z. Pei, Z. Wang, Q. Xue, X. Xie, C. Zhi, A self-healable and highly stretchable supercapacitor based on a dual crosslinked polyelectrolyte. *Nat. Commun.* **6**, 10310 (2015).
42. L. Han, L. Yan, K. Wang, L. Fang, H. Zhang, Y. Tang, Y. Ding, L.-T. Weng, J. Xu, J. Weng, Y. Liu, F. Ren, X. Lu, Tough, self-healable and tissue-adhesive hydrogel with tunable multifunctionality. *NPG Asia Mater.* **9**, –e372 (2017).
43. D. Zhang, X. Zhang, Y. Chen, P. Yu, C. Wang, Y. Ma, Enhanced capacitance and rate capability of graphene/polypyrrole composite as electrode material for supercapacitors. *J. Power Sources* **196**, 5990–5996 (2011).
44. L. Ding, Y. Wei, L. Li, T. Zhang, H. Wang, J. Xue, L.-X. Ding, S. Wang, J. Caro, Y. Gogotsi, MXene molecular sieving membranes for highly efficient gas separation. *Nat. Commun.* **9**, 155 (2018).
45. X. Yan, Z. Liu, Q. Zhang, J. Lopez, H. Wang, H.-C. Wu, S. Niu, H. Yan, S. Wang, T. Lei, J. Li, D. Qi, P. Huang, J. Huang, Y. Zhang, Y. Wang, G. Li, J. B.-H. Tok, X. Chen, Z. Bao, Quadruple H-bonding cross-linked supramolecular polymeric materials as substrates for stretchable, antitearing, and self-healable thin film electrodes. *J. Am. Chem. Soc.* **140**, 5280–5289 (2018).
46. S. He, F. Zhang, S. Cheng, W. Wang, Synthesis of sodium acrylate and acrylamide copolymer/GO hydrogels and their effective adsorption for Pb^{2+} and Cd^{2+}. *ACS. Sustainable Chem. Eng.* **4**, 3948–3959 (2016).
47. M. Zhu, Y. Huang, Q. Deng, J. Zhou, Z. Pei, Q. Xue, Y. Huang, Z. Wang, H. Li, Q. Huang, C. Zi, Highly flexible, freestanding supercapacitor electrode with enhanced performance obtained by hybridizing polypyrrole chains with MXene. *Adv. Energ. Mater.* **6**, 1600969 (2016).
48. C. J. Zhang, S. Pinilla, N. McEvoy, C. P. Cullen, B. Anasori, E. Long, S.-H. Park, A. S. Seral-Ascaso, A. Shmeliov, D. Krishnan, C. Morant, X. Liu, G. S. Duesberg, Y. Gogotsi, V. Nicolosi, Oxidation stability of colloidal two-dimensional titanium carbides (MXenes). *Chem. Mater.* **29**, 4848–4856 (2017).
49. L. Ding, Y. Wei, Y. Wang, H. Chen, J. Caro, H. Wang, A two-dimensional lamellar membrane: MXene nanosheet stacks. *Angew. Chem. Int. Ed.* **56**, 1825–1829 (2017).
50. Y.-J. Liu, W.-T. Cao, M.-G. Ma, P. Wan, Ultrasensitive wearable soft strain sensors of conductive, self-healing, and elastic hydrogels with synergistic "soft and hard" hybrid networks. *ACS Appl. Mater. Interfaces* **9**, 25559–25570 (2017).
51. J. M. González-Domínguez, C. Martín, O. S. J. Durá, S. Merino, E. Vázquez, Smart hybrid graphene hydrogels: A study of the different responses to mechanical stretching stimulus. *ACS Appl. Mater. Interfaces* **10**, 1987–1995 (2018).
52. S. Liu, L. Li, Ultrastretchable and self-healing double-network hydrogel for 3D printing and strain sensor. *ACS Appl. Mater. Interfaces* **9**, 26429–26437 (2017).
53. Z. Lei, Q. Wang, S. Sun, W. Zhu, P. Wu, A bioinspired mineral hydrogel as a self-healable, mechanically adaptable ionic skin for highly sensitive pressure sensing. *Adv. Mater.* **29**, 1700321 (2017).
54. F. Lin, Z. Wang, Y. Shen, L. Tang, P. Zhang, Y. Wang, Y. Chen, B. Huang, B. Lu, Natural skin-inspired versatile cellulose biomimetic hydrogels. *J. Mater. Chem. A* **7**, 26442–26455 (2019).
55. X. Wang, T. Li, J. Adams, J. Yang, Transparent, stretchable, carbon-nanotube-inlaid conductors enabled by standard replication technology for capacitive pressure, strain and touch sensors. *J. Mater. Chem. A* **1**, 3580–3586 (2013).

Acknowledgments: V.T. is beholden to K. Chuang for visual aesthetics. We thank R. Sun, L. Cai, and Y. Shao for assistance and discussions. **Funding:** Y.C., C.-W.Y., K.-W.H., and V.T. acknowledge the support from KAUST Catalysis Center (KCC) and the Physical Science Engineering (PSE) division. A.A.A. and J.-H.F. are indebted to the support from the KAUST Solar Center (KSC), Office of Sponsored Research (OSR) under award no. OSR-2018-CARF/CCF-3079. S.J.J. was supported by NIH Common Fund through an NIH Director's Early Independence Award cofunded by the National Institute of Dental and Craniofacial Research and Office of the Director, NIH, under award number DP5OD028181. S.J.J. also acknowledges Young Investigator Award funds from the Alex's Lemonade Stand Foundation for Childhood Cancer Research, the Hyundai Hope on Wheels Foundation for Pediatric Cancer Research, and the Tower Cancer Research Foundation. **Author contributions:** Y.C., J.S., and C.-W.Y. fabricated e-skin devices. V.T. and X.D. suggested and supervised the project. H.-L.T. provided capacitive device measurements. Y.W. and A.A.A. performed materials characterization. C.C. and J.S. provided TEM analysis. Y.C., J.S., S.J.J., Y.H., J.-H.F., X.W., and K.-W.H. analyzed the results and developed the explanation of the experiment. Y.C., J.S., S.J.J., and V.T. wrote the manuscript. All of the authors contributed to discussions. **Competing interests:** The authors declare that they have no competing interests. **Data and materials availability:** All data needed to evaluate the conclusions in the paper are present in the paper and/or the Supplementary Materials. Additional data related to this paper may be requested from the authors.

Submitted 3 March 2020
Accepted 16 October 2020
Published 27 November 2020
10.1126/sciadv.abb5367

Citation: Y. Cai, J. Shen, C.-W. Yang, Y. Wan, H.-L. Tang, A. A. Aljarb, C. Chen, J.-H. Fu, X. Wei, K.-W. Huang, Y. Han, S. J. Jonas, X. Dong, V. Tung, Mixed-dimensional MXene-hydrogel heterostructures for electronic skin sensors with ultrabroad working range. *Sci. Adv.* **6**, eabb5367 (2020).